# Magnetic properties and noncollinear spin structure of the tin-rich stannide Ho$_5$Co$_6$Sn$_{18}$

Chin-Wei Wang [1,*] Sunil K. Karna [2,†] Shin-ichiro Yano,[1] Chi-Hung Lee,[1,3] Maxim Avdeev,[4,5] Chin Shan Lue,[6,7,8] and Chia Nung Kuo[6,7,8]

[1]*National Synchrotron Radiation Research Center, Hsinchu 30077, Taiwan*
[2]*Quantum Electronics Group, Department of Physics and Center for Materials Research, Norfolk State University, Norfolk, Virginia 23504, USA*
[3]*Department of Applied Physics, Tunghai University, Taichung 40704, Taiwan*
[4]*Australian Nuclear Science and Technology Organisation, New Illawarra Road, Lucas Heights, New South Wales 2234, Australia*
[5]*School of Chemistry, The University of Sydney, Sydney 2006, Australia*
[6]*Department of Physics, National Cheng Kung University, Tainan 70101, Taiwan*
[7]*Taiwan Consortium of Emergent Crystalline Materials, Ministry of Science and Technology, Taipei 10601, Taiwan*
[8]*Program on Key Materials, Academy of Innovative Semiconductor and Sustainable Manufacturing, National Cheng Kung University, Tainan 70101, Taiwan*

We have investigated the magnetic, structural, and thermodynamic properties of Ho$_5$Co$_6$Sn$_{18}$ through x-ray and neutron diffraction, magnetization, and specific heat measurements. Ho$_5$Co$_6$Sn$_{18}$ displays a magnetic transition at $T_M = 3.4$ K and can be described with the magnetic space group $I4_1/ac'd'$. The two holmium sublattices Ho(1) and Ho(2) exhibit different magnetic behaviors. Ferromagnetic order on the Ho(1) site develops into a net magnetization along the $c$ axis below $T_M$. In contrast, the ordering of the Ho(2) site is determined by geometric magnetic frustrations. The Ho(2) spins order into the noncollinear, two-in-two-out antiferromagnetic pattern on the Ho(2)$_4$ tetrahedron. At 60 mK, the ordered moment of Ho(2) reaches 4.01 (8) $\mu_B$, which is about half of the Ho(1) moment. Upon the application of a magnetic field, ferromagnetic components along the $c$ axis are induced on Ho(2), along with the in-plane antiferromagnetic components, indicating the XY-like spin anisotropy of the Ho(2) spins. A magnetic quasielastic neutron scattering signal is observed above $T_M$ and significantly weakens with the magnetic ordering.

## I. INTRODUCTION

Geometrically frustrated antiferromagnets have been popular research subjects in the past decades and their magnetic sublattice composed of regular polygons exhibit dominant antiferromagnetic nearest-neighbor exchange couplings [1]. The antiferromagnetic interactions among spins residing on such polygons, e.g., planar triangles and triangular faces of tetrahedra, compete and the spin system cannot reach a single ground state to satisfy all the magnetic interactions. As a result, many ground states with similar energies might exist simultaneously, which prevents the long-range magnetic order and often leads to novel low-temperature magnetic phases like spin glass, spin liquid, and spin ice. The famous pyrochlore $A_2B_2X_7$ family compounds, which allow for many combinations of $A$ and $B$ ions, are mostly studied geometrically frustrated antiferromagnet [2]. The novel low-temperature phenomena such as dipolar spin ice (Ho$_2$Ti$_2$O$_7$ and Dy$_2$Ti$_2$O$_7$), spin liquid (Tb$_2$Ti$_2$O$_7$), and spin glass (Ca$_2$Ru$_2$O$_7$) are realized on the corner-sharing tetrahedra sublattice [3–6]. It was speculated that the conduction electron-mediated coupling of localized spins, the so-called Ruderman-Kittel-Kasuya-Yosida (RKKY)

interaction, is similar to the dipolar interaction [7]. Like the dipolar interactions in Ho$_2$Ti$_2$O$_7$ and Dy$_2$Ti$_2$O$_7$, the RKKY interaction might also stabilize spin ice behavior in the intermetallic compounds containing the rare-earth ions with a large magnetic moment.

In a search for the geometrically frustrated magnets in intermetallic compounds, the ternary intermetallic stannides, RE$M_x$Sn$_y$ ($M$ = Rh, Co, Ir, and Ru), attracted our attention. The family of ternary intermetallic stannides, RE$M_x$Sn$_y$ ($M$ = Rh, Co, Ir, and Ru), was reported in the 1980s [8]. Up to five different structure types are realized in the stannides family. Among them, the phase-II or 5-6-18 compound is most attractive due to the inherent tetrahedral sublattice of the rare-earth spins. RE$_5M_6$Sn$_{18}$ crystallizes in the tetragonal $I4_1/acd$ (no. 142) space group with eight chemical formula units in a unit cell. The structure type has been thoroughly studied from the crystal chemistry point of view, concerning the coordination and bond lengths [9,10]. The crystal structure features a complex 3D structure built of alternately stacking two types of two-dimensional (2D) slabs composed of corner-sharing CoSn$_6$ trigonal prisms. The rare-earth ions reside in the voids of the 3D network occupying two inequivalent crystallographic sites. Both rare-earth sites feature tetrahedral arrangements that influence the magnetic behaviors of RE$_5M_6$Sn$_{18}$. For example, the Curie-Weiss constant $\theta_{CW}$, which depends on the sum of all exchange interactions

---
*wang.cw@nsrrc.org.tw
†skkarna@nsu.edu

in the mean-field theory, is very close to zero in $Tm_5Co_6Sn_{18}$ and $Er_5Co_6Sn_{18}$ [11], indicating weak magnetic couplings or competitive ferromagnetic and antiferromagnetic exchange couplings of comparable magnitudes. Both cases exhibit very low magnetic ordering temperatures. For example, the reentrant superconductor $ErRh_{1.1}Sn_{3.6}$ of the phase-II structure enters the superconducting state below the $T_{critical} = 1.36$ K on cooling and then returns to the normal state again below the ferromagnetic Curie temperature $T_C = 0.46$ K [12]. The spin-glass behavior due to the competition between ferromagnetic and antiferromagnetic magnetic couplings was reported in $HoRh_{1.2}Sn_{3.9}$ and $Dy_5Co_6Sn_{18}$ with the freezing temperature of 1.7 and 6.5 K, respectively [13,14]. On the contrary, $Ho_5Co_6Sn_{18}$ has been reported as an outlier having ferromagnetic $T_C = 127$ K, antiferromagnetic $T_N = 7.6$ K, and Curie-Weiss constant $\theta_{CW} = 50.9$ K [15]. However, our experimental results indicate that $Ho_5Co_6Sn_{18}$ is not an outlier.

Furthermore, the field-dependent magnetization curves $\mathbf{M}(H)$ of $RE_5Co_6Sn_{18}$ (RE = Dy, Ho, Er, Tm) display a rapid rise in the low field regime and nonsaturation behavior, indicating that the ferromagnetic and antiferromagnetic exchange couplings coexist in these compounds. Last, the effective moments for $Tm_5Co_6Sn_{18}$, $Er_5Co_6Sn_{18}$, $ErRh_{1.1}Sn_{3.6}$, $Dy_5Co_6Sn_{18}$, and $Ho_5Co_6Sn_{18}$ are $8.82\,\mu_B$, $7.9\,\mu_B$, $8.66\,\mu_B$, 10.61, and $8.19\,\mu_B$, respectively [11–15]. These values are close to or slightly smaller than the expected values for the trivalent rare-earth ions, which indicates that the rare earth elements are the dominant magnetic species in these compounds. Herein, we report the bulk magnetic properties, specific heat, neutron powder diffraction, and inelastic neutron scattering results of $Ho_5Co_6Sn_{18}$. Neutron powder diffraction experiments reveal that the two holmium sublattices exhibit different magnetic behaviors. The Ho(1) order ferromagnetically whereas the Ho(2) spins order into the noncollinear, two-in-two-out antiferromagnetic pattern on the $Ho(2)_4$ tetrahedron.

## II. EXPERIMENTAL DETAILS

Single crystals of $Ho_5Co_6Sn_{18}$ were synthesized by the Sn-flux method [16]. High-purity Ho ingots (99.5%), Co powder (99.9%), and Sn ingots (99.999%) were mixed in the ratio of 1:1.2:40 and sealed in an evacuated quartz tube with a flat bottom. The mixed elements were heated to 1050° C for 12 h, dwelled for 20 h, then cooled down to 500 °C in 150 h. Excess Sn flux was separated from the crystals by centrifugation and by etching in dilute HCl. The smaller crystals from multiple batches of preparations were crushed, well ground into fine powders, and checked by x-ray powder diffraction (Bruker D2) before being mixed as the sample for the neutron powder diffraction (NPD) measurements.

Magnetization measurements were performed on polycrystalline and single-crystalline $Ho_5Co_6Sn_{18}$ samples using the Physical Properties Measurement System (PPMS, Quantum Design) and Magnetic Properties Measurement System (MPMS, Quantum Design). Specific heat experiments were conducted using the calorimeter insert of a Physical Property Measurement System (Quantum Design) operating with a dilution refrigerator to reach 0.2 K.

Neutron powder diffraction (NPD) experiments were conducted on the high-resolution powder diffractometer, ECHIDNA [17], and the high-intensity powder diffractometer, WOMBAT [18] at the OPAL reactor, ANSTO. In the ECHIDNA part, 2.4395-Å neutrons defined by Ge (331) crystals at a 140° take-off angle were used. The closed-cycle cryostat and the dilution refrigerator were employed for data collection down to 1.5 K and 60 mK, respectively. In the ultralow-temperature NPD experiment, the slurry of $Ho_5Co_6Sn_{18}$ and deuterated isopropanol were loaded into an oxygen-free copper can to maximize heat exchange under vacuum, whereas the vanadium sample can was used in the neutron scattering experiments down to 1.5 K in a cryostat filled with exchange He gas. The FULLPROF Suite [19] was used for Rietveld analysis and magnetic structure determination. The Bilbao Crystallographic Server was employed for identifying the magnetic space group [20–22]. The magnetic field-dependent NPD patterns were collected on WOMBAT with the 12-T asymmetrical vertical cryomagnet. 2.41-Å neutrons defined by Ge (115) crystals at 90° take-off angle were used in the field-dependent NPD measurements.
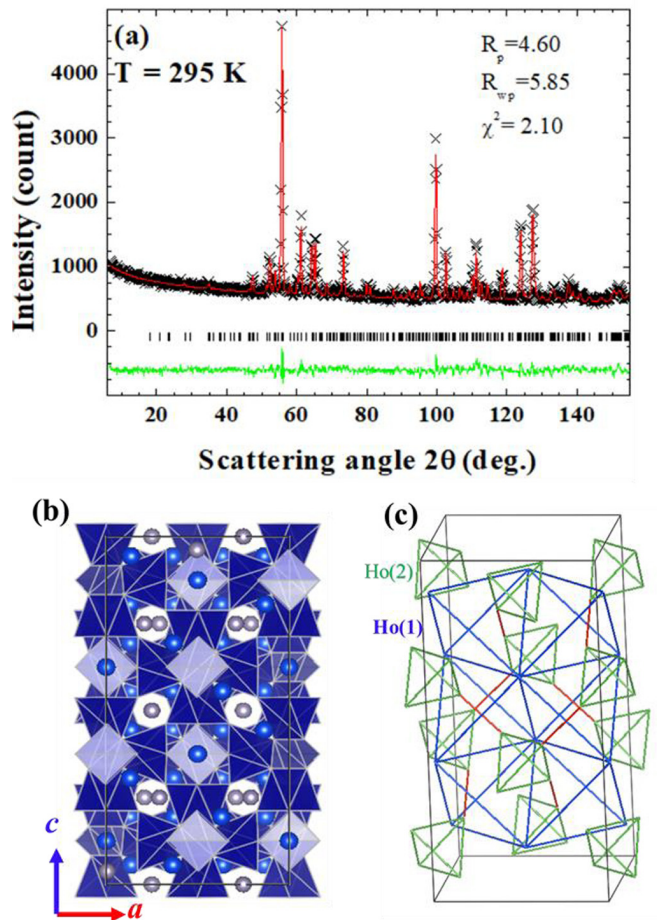


FIG. 1. (a) Neutron powder diffraction patterns of $Ho_5Co_6Sn_{18}$ measured at 295 K ($\lambda = 2.4395$ Å). (b) Polyhedral view of $Ho_5Co_6Sn_{18}$ crystal structure. (c) Magnetic sublattice of $Ho_5Co_6Sn_{18}$. Blue and green lines represent the Ho(1) and Ho(2) tetrahedrons, respectively. The red lines indicate the shortest Ho(2)-Ho(2). All atoms are omitted for clarity.
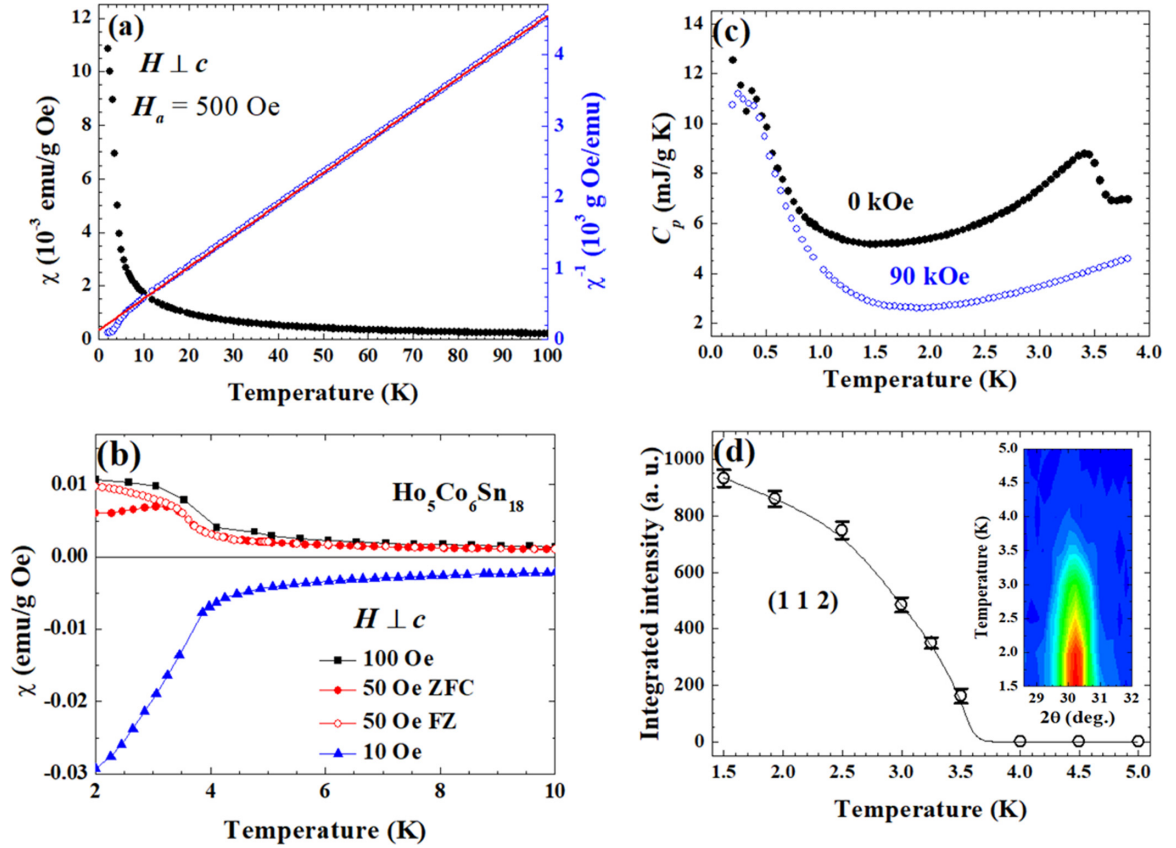
FIG. 2. (a) The magnetic susceptibility $\chi(T)$ curve of $Ho_5Co_6Sn_{18}$. The $\chi^{-1}(T)$ curve is plotted in the right axis, and the red line is the linear fit to the data point above 30 K. (b) $M(T)$ curves measured in a magnetic field of 10, 50, and 100 Oe. (c) Temperature dependence of the heat capacity of $Ho_5Co_6Sn_{18}$ measured without a magnetic field and in a magnetic field of 90 kOe. (d) Temperature dependence of the integrated intensities of the purely magnetic (1 1 2) peak. The inset shows the color contour of the (1 1 2) peak. The line is guide for eyes.

We also measured the magnetic order parameter and the inelastic scattering signals from the polycrystalline sample on the cold triple-axis spectrometer, SIKA, at the OPAL reactor, ANSTO [23,24]. An ILL liquid He orange cryostat was used to cool the sample down to $\sim 1.55$ K. The $E_f$ was fixed to 5 meV, and a cold Be filter was installed on the scattering side in both the elastic and inelastic scattering measurements.

## III. RESULTS AND DISCUSSION

The crystal structure of the synthesized compound is confirmed with the x-ray and neutron diffraction. The NPD pattern at 300 K [Fig. 1(a)] can be fitted well with a $Tb_5Rh_6Sn_{18}$-type structure having tetragonal space group $I4_1/acd$ (no. 142), yielding lattice constant $a = b = 13.5484(2)$ Å and $c = 27.0386(9)$ Å at room temperature. The schematic crystal structure of $Ho_5Co_6Sn_{18}$ is shown in Fig. 1(b). Slightly distorted $CoSn_6$ trigonal prisms form the framework, and the holmium atoms and Sn(6) sit in the voids. The holmium atoms occupy two distinct sites, Ho(1) at 8$b$ and Ho(2) at 32$g$. Ho(1) is surrounded by 12 tin atoms: 2 Sn(1), 4 Sn(2), 4 Sn(3), and 2 Sn(4), forming the Ho(1)$Sn_{12}$ cuboctahedron. On the other hand, each Ho(2) is coordinated with nine tin atoms: 1 Sn(1), 2 Sn(2), 2 Sn(3), 1 Sn(4), and 3 Sn(5). Four Ho(2)$Sn_9$ triangular cupolas are connected by

sharing the Sn(5) atoms to form the Ho(2)$_4$ tetrahedral clusters. The $CoSn_6$ and $RESn_{12}$ are also the building blocks in the $RE_3M_4Sn_{13}$ stannides [25].

Holmium is the dominant magnetic element in the compound, so that it is worth emphasizing the holmium sublattice here. Ho(1) ions reside on a face-center-tetragonal lattice with $c/a = 0.998$. Each Ho(1) has 12 neighboring Ho(1), forming edge-sharing tetrahedrons with the edge length of $\sim 9.5$ Å, as illustrated by the blue lines in Fig. 1(c). Such magnetic sublattice, despite the slight tetrahedral distortion, is similar to the magnetic sublattice of a disordered fluorite structure, which possesses the features of the magnetic disorder and magnetic frustrations [26]. On the other hand, the Ho(2)$_4$ tetrahedra [green lines in Fig. 1(c)] have an edge length of $\sim 5.2$ Å. In addition, the Ho(2)$_4$ units and Ho(1) atoms compose the rocksalt structure. However, strictly speaking, the Ho(2)$_4$ tetrahedra are not isolated due to the presence of the shorter Ho(2)-Ho(2) bonds $\sim 5$ Å [red lines in Fig. 1(c)] along the pseudocubic diagonal.

The temperature dependence of the magnetic susceptibility $\chi(T)$ of $Ho_5Co_6Sn_{18}$ is presented in Fig. 2(a). The $M(T)$ increases while cooling without showing any anomalies like observed for $Dy_5Co_6Sn_{18}$ [14]. In addition, the $\chi^{-1}(T)$ deviates downward from the high-temperature Curie-Weiss behavior, indicating of increasing ferromagnetic correlations.

The fit with the Curie-Weiss law to the data yields the slightly negative Curie-Weiss temperature, $\theta_{CW}$ of $-3.01(5)$ K and effective moment, $\mu_{eff}$ of $10.95(1)\mu_B$/Ho. The obtained $\mu_{eff}$ is close to the theoretical value of $10.61\,\mu_B$/Ho$^{3+}$ for the $^5I_8$ ground state ($g = 5/4$ and $J = 8$).

Figure 2(b) shows $\chi(T)$ curves measured from a single crystal sample. The $\chi(T)$ curve at $H_a = 10$ Oe shows the negative diamagnetic response of the metallic compound and a further drop of magnetization due to the superconducting Meissner effect of the residual Sn flux. The ferromagnetic signal becomes evident when the applied magnetic field suppresses the superconductivity of tin (the critical field $H_{c0} \sim$ 300 Oe). The bifurcation of field cooled and zero field cooled magnetization data measured with 50 Oe reveals evident ferromagnetic transition. As shown in Fig. 2(c), a peak appears in $C_p(T)$ at $\sim 3.4$ K, which is slightly lower than the superconducting temperature of tin ($T_c = 3.7$ K). In addition, the specific heat associated with the superconducting transition of tin is $\sim 7.2\,\mu J$/gK which is negligible in the data [27]. Therefore, the peak in $C_p(T)$ is associated with the long-range magnetic ordering in the compound, which is confirmed by the order parameter from NPD [Fig. 2(d)]. We do not observe any anomaly in our data at 127 or 7.6 K, which have been reported by Zeng *et al.* [15].

The field dependence of the magnetization of a single crystal sample measured at 2 and 5 K is plotted in Fig. 3. We do not observe the saturation up to 90 kOe. At $T = 2$ K, the magnetic moment reaches $7.73\,\mu_B$/Ho at $H_a = 70$ kOe, presuming only the Ho ions contribute to the magnetization. The highest value of magnetization we observed in the polycrystalline sample is $7.62\,\mu_B$/Ho at $H_a = 90$ kOe and $T = 2.5$ K (see Fig. S1 in the Supplemental Material [28]). The ferromagnetic component in Ho$_5$Co$_6$Sn$_{18}$ is evidenced by the low-field regime of the $M(H)$ curves, as shown in Fig. 3(b). At $T = 2$ K, the $M(H)$ curves of both $H//c$ and $H \perp c$ show a quick rise and then become linear to the magnetic field at $\sim 1.5$ kOe. In contrast, the magnetization increases linearly to the magnetic field of both the field directions at $T = 5$ K. The magnetization is always higher with $H//c$ than $H \perp c$, indicating the ferromagnetic component is along the $c$ axis. The nonsaturated character indicates strong antiferromagnetic couplings or single-ion anisotropy.

Figure 4 shows the neutron powder diffraction patterns collected at 5 and 15 K and the refined structural parameters are listed in Table S1 of the Supplemental Material [28]. The crystal structure at 5 K is the same as that at 295 K. New peaks appear in the diffraction pattern and confirm the long-range magnetic order at 1.5 K. These peaks can be indexed with a commensurate propagation vector $q = (0, 0, 0)$. We use the MAXMAGN of the Bilbao crystallographic server to obtain the maximal magnetic groups of the paramagnetic $I4_1/acd$ space group, which yielded 12 maximal magnetic space groups allowing nonzero magnetic moments for at least one of the two Ho sites. The magnetic space group $I4_1/ac'd'$ (BNS no. 142.567) is identified as providing the best agreement after testing all the possible models one by one against the data using the FULLPROF program. In the magnetic structure, the Ho(1) moments at the $8b$ site all aligned with the **c** axis, resulting in a nonzero net ferromagnetic moment. On the other hand, the Ho(2) spins on a Ho(2)$_4$ tetrahedra are constrained
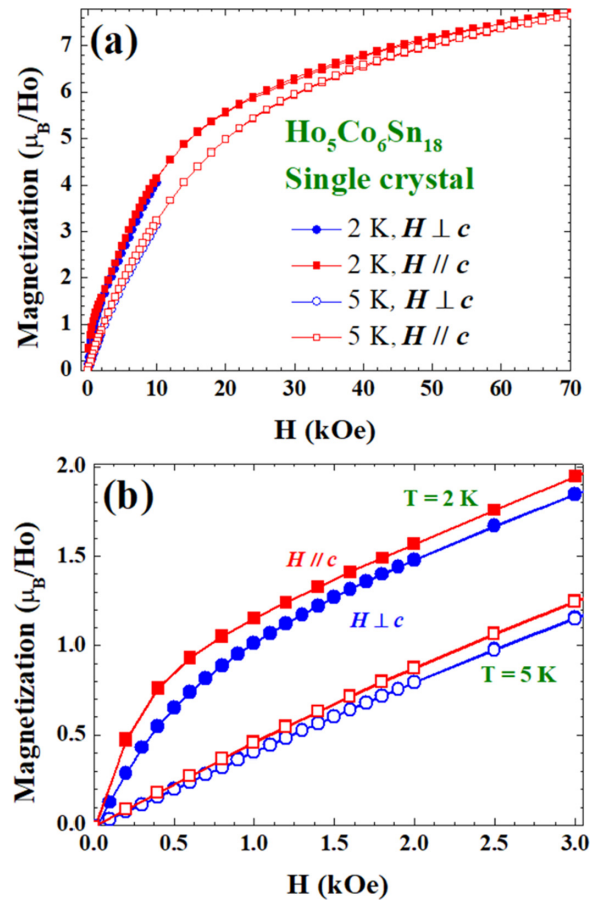


FIG. 3. (a) Field dependence of the magnetization with the magnetic field applied along and perpendicular to the $c$ axis, at 2 and 5 K. (b) Zoom-in view of the low-field regime illustrates the existence of ferromagnetic component.

as $(Mx, My, Mz)$, $(-Mx, -My, Mz)$, $(My, -Mx, Mz)$, and $(-My, Mx, Mz)$. As a result, the Ho(2) sublattice adopts the two-in-two-out configuration in the $ab$ plane and allows a net magnetization along the $c$ axis. Surprisingly, we do not observe significant ordered moments on the $32g$ site. Assigning the ordered moments to Ho(2) site would produce additional peaks, such as (1 0 1) and (1 1 0), which are absent at 1.5 K. The refined magnetic moment of Ho(1) is $7.89(8)\,\mu_B$ along the $c$-axis. The ordered Ho(2) moment is estimated to be smaller than $\sim 0.2\,\mu_B$ at 1.5 K. We measured the purely magnetic (1 1 2) peak as a function of temperature using the triple-axis spectrometer SIKA. Figure 2(d) plots the peak intensity variation, showing that the long-range magnetic order temperature $T_M$ at $\sim 3.5$ K.

To investigate the unusual site-selective magnetic ordering further, we cool the sample down to 60 mK. Additional magnetic diffraction peaks, such as (1 0 1) and (1 1 0), appear in the NPD pattern collected at 60 mK. We find that low-temperature magnetic Bragg peaks can be generated by activating the magnetic moments of Ho(2) transformed according to the same $I4_1/ac'd'$ magnetic space group, where the Ho(2) spins on tetrahedron adopt the two-in-two-out configuration in the $ab$ plane, but allow a net magnetization along the **c** axis. Unfortunately, the NPD patterns are highly
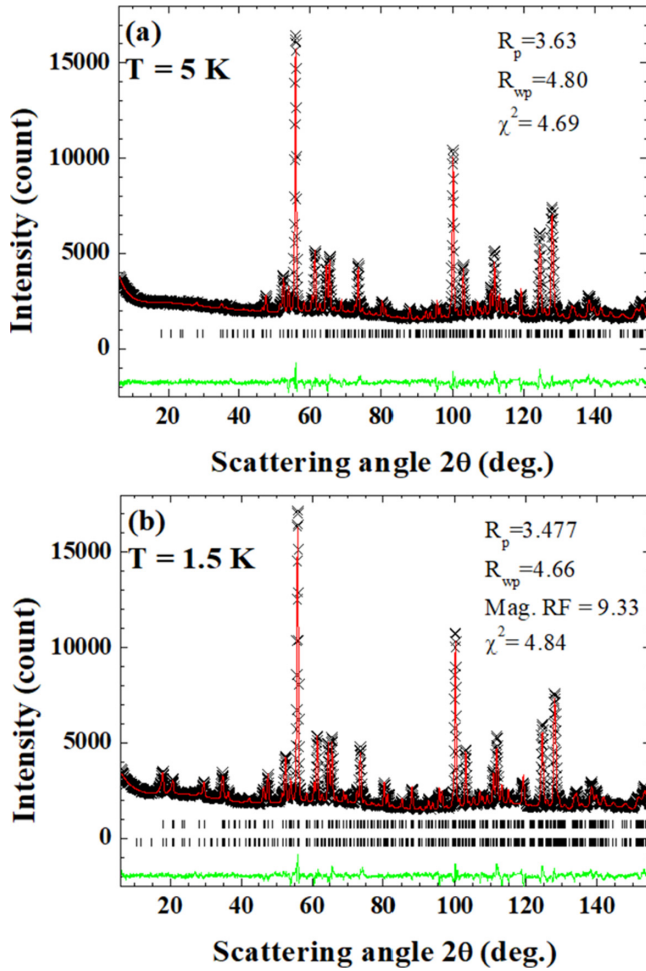
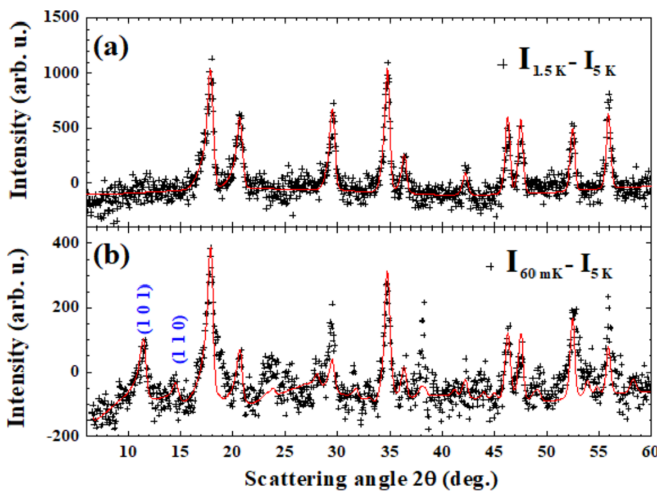FIG. 4. Neutron powder diffraction patterns of $Ho_5Co_6Sn_{18}$ measured at (a) 5 K, and (b) 1.5 K, $\lambda = 2.4395$ Å.



FIG. 5. Magnetic diffraction of $Ho_5Co_6Sn_{18}$ of (a) 1.5 K ($\chi2 = 1.11$, $R_{mag} = 16.58$), and (b) 60 mK ($\chi2 = 4.26$, $R_{mag} = 27.47$), obtained by subtracting the 5-K NPD patterns as the backgrounds. Rietveld refined fit to the magnetic diffraction profile using the $I4_1/ac'd'$ magnetic space group.

contaminated by the isopropanol ice (see Fig. S2 [28]). We therefore analyzed the pure magnetic diffraction pattern by subtracting the 5-K pattern from the 60-mK data. The fitting of the purely magnetic diffraction pattern is shown in Fig. 5(b). The three magnetic moment components obtained by fitting the magnetic diffraction pattern are $M_x = -1.23(10)$, $M_y = -3.82(10)$, and $M_z = -0.022(115) \mu_B$. The small value and significant error of $M_z$ suggest that the Ho(2) moments lie in the $ab$ plane and contribute negligible magnetization. The magnetic structure at 60 mK is plotted in Fig. 6, where the ordered magnetic moments of Ho(1) and Ho(2) are 7.93(16) $\mu_B$ along the $c$ axis and 4.01(8) $\mu_B$ in the $ab$ plane, respectively.

The NPD patterns were measured under various magnetic fields and temperatures (Fig. 7). We collected data at $H = $ 10, 30, 50, 70, and 90 kOe, at $T = 2$ K. Then we retained the 90-kOe field and measured the patterns as a function of temperature up to 110 K. The magnetic field significantly influences the diffraction patterns. First, the incoherent magnetic scattering is largely reduced by the magnetic field, a typical feature of spins being polarized. Second, the magnetic Bragg peaks associated with the order of Ho(2) spins appear in the patterns above 10 kOe, indicating that the Ho(2) spins are polarized by the external magnetic field. Because the powder was not pelletized and the compound possesses ferromagnetic magnetization along the $c$ axis, the applied field resulted in particle reorientation. As a result, the most pronounced (1 1 2) magnetic peak is almost undetectable upon applying the magnetic field. We assumed the same $I4_1/ac'd'$ magnetic symmetry and employed the modified March's function with the preferred orientation vector (0 0 1). Although the simple uniaxial model cannot perfectly correct the texture distribution in the current case, we still get a reasonable fit and catch the major effects exerted by the magnetic field. The Rietveld plots of NPD patterns under magnetic fields and preferred orientation parameters are summarized in Fig. 8. The magnetic moment of the Ho(1) linearly increases with the applied magnetic field from $\sim 7.9$ to $\sim 9.3 \mu_B$, whereas the Ho(2) spins are induced from zero to $\sim 9.5 \mu_B$, as shown in Fig. 9(a). However, the antiferromagnetic $M_x$ and $M_y$ components grow simultaneously with the ferromagnetic $M_z$ component. As a result, the Ho(2) spins maintain an angle of $\sim 54°$ to the $ab$ plane between $H = 10$ and 90 kOe [Figs. 9(b) and 9(c)]. It is likely resulted from the balance between the in-plane magnetic anisotropy of Ho(2) and the external field, reducing the spin fluctuation rather than deflecting from the easy plane. The net magnetization of Ho(1) and Ho(2) are parallel so that the net magnetization at $T = 2$ K and $H = 90$ kOe is $0.2 \times 9.309 + 0.8 \times 7.839 = 8.133 \mu_B$/Ho, which is not too far from $7.62 \mu_B$/Ho obtained by magnetometry from the powder sample at $T = 2.5$ K and $H = 90$ kOe. When thermal agitation increases with temperature, the field-induced magnetic moments reduce, as shown in the right-half of Figs. 9(a)–9(c). The magnitudes of Ho(1) and Ho(2) spins exhibit very similar thermal relaxation. Besides, the $M_x$ and $M_y$ components decay faster than the $M_z$ does, indicating that the in-plane anisotropy of Ho(2) is getting weaker during warming so that the field-induced static moment of Ho(2) lifts to $\sim 75°$ to the $ab$ plane at 110 K.
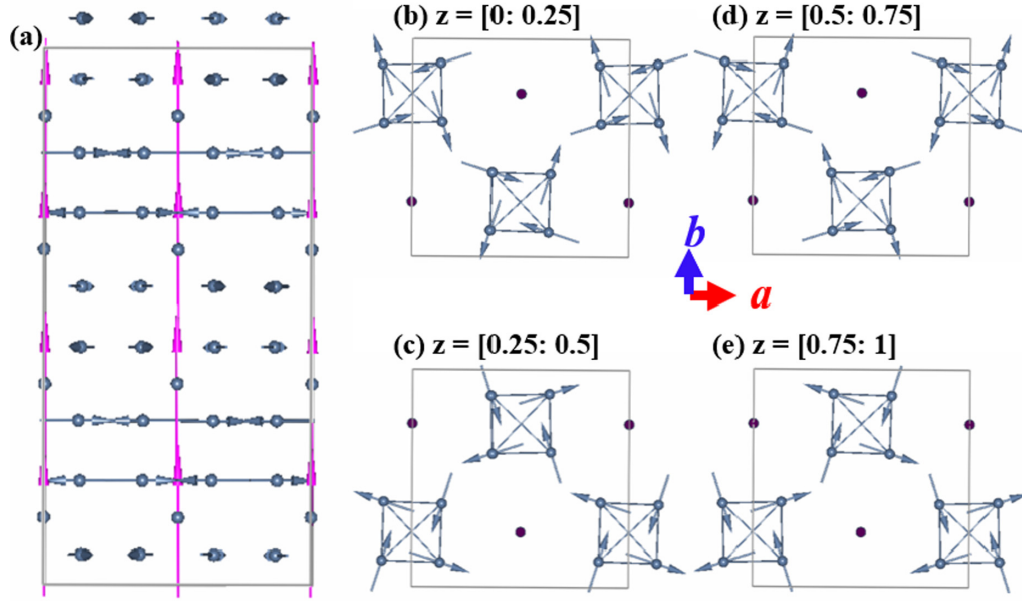
FIG. 6. (a) Magnetic structure at 60 mK shows the Ho(1) spin pointing along the $c$-axis and the Ho(2) spins lying in the $a$-$b$ plane. Panels (b)−(e) show the magnetic structure viewed along the $c$ axis sliced into four layers: (b) $z = [0 : 0.25]$, (c) $z = [0.25 : 0.5]$, (d) $z = [0.5 : 0.75]$, and (e) $z = [0.75 : 1]$.
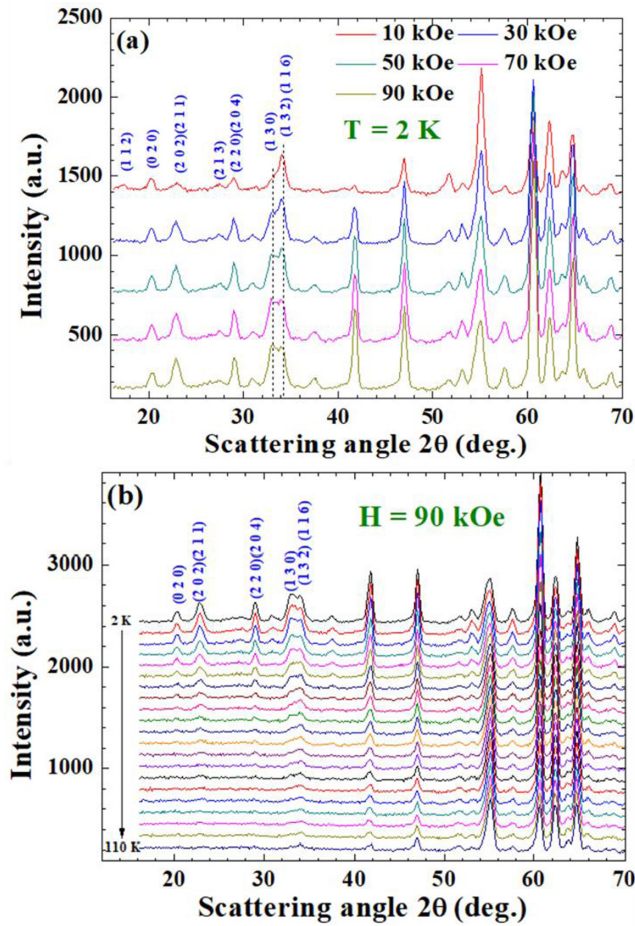


FIG. 7. (a) NPD patterns measured at 10, 30, 50, 70, and 90 kOe at $T = 2$ K (b) NPD patterns measured upon warming to 110 K in a magnetic field of 90 kOe.

Searching for more features of the magnetic frustration, we conducted the inelastic neutron scattering measurements on $Ho_5Co_6Sn_{18}$ crystal powder sample. Constant-$q$ energy scans were performed around the purely magnetic (1 1 2) peak, at $q = 0.809$, 0.7, and 0.52 Å$^{-1}$, as shown in Fig. 10. Two excitations are identified at $E = 0.345(4)$ meV and 1.467(11) meV. The peak positions are $q$ independent, and the intensities become slightly more intense at low $q$. Both peaks persist above $T_M$ [see Fig. 10(c)]. Hence, the two excitations are not the spin-wave associated with the magnetic order of Ho(1) but should be the crystal field levels of $Ho^{3+}$. In addition, the quasielastic scattering (QENS) centered at zero energy transfer, $E = 0$, exists at $T = 5$ K and makes the elastic line broader. The QENS becomes weaker at $T = 1.6$ K but still persists. In strongly frustrated magnetic compounds, above the long-range ordering or glass-freezing temperatures, the spin systems set into the cooperative paramagnetic phase with a short-range magnetic correlation both in space and time, manifested as the modulated background and the quasielastic neutron scattering in neutron scattering, respectively. Intriguingly, the observed quasielastic scattering is associated with Ho(1) rather than Ho(2) with the isolated tetrahedral arrangement, given that the Ho(2) moment is far smaller than the expected full moment at 1.6 K.

## IV. CONCLUSIONS

Compounds containing structural units that approximate the ideal tetrahedral arrangements of antiferromagnetically coupled magnetic atoms are associated with geometric frustration. Two types of tetrahedral sublattices exist in $Ho_5Co_6Sn_{18}$. Both are potentially magnetically frustrated, despite both being slightly distorted. However, $Ho_5Co_6Sn_{18}$ is not regarded as a frustrated magnet for its small frustration parameter $|\theta_{CW}/T_N| \sim 0.9$, according to Ramirez's definition of
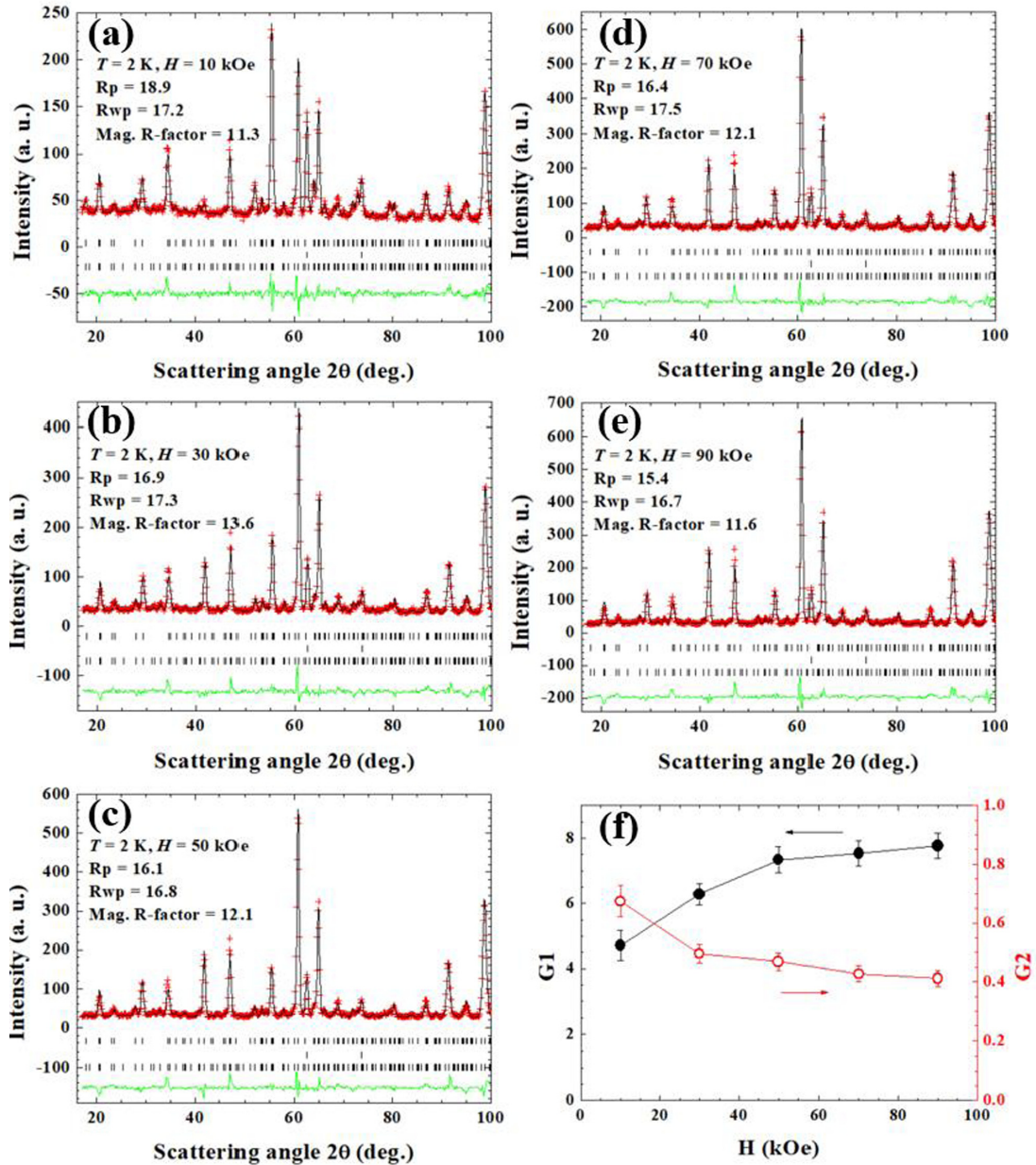
FIG. 8. Rietveld plots of the NPD pattern measured under (a) 10 kOe, (b) 30 kOe, (c) 50 kOe, (d) 70 kOe, and (e) 90 kOe. The modified March function was employed with the preferred orientation vector (0 0 1). (f) The preferred orientation parameters $G1$ (degree of preferred orientation) and $G2$ (the fraction of the sample that is not textured) are plotted as a function of applied magnetic field.

magnetic frustration [29]. Indeed, long-range magnetic ordering develops below a not-too-low temperature of $T_M = 3.4$ K. The Ho(1) spins develop a ferromagnetic order with the moments along the **c** axis, whereas the more closely spaced Ho(2) spins remain fluctuating down to at least 1.5 K. Even on cooling down to 60 mK, the ordered moment of Ho(2) is merely $4.01(8)\,\mu_B$, about 50% of the moment of Ho(1). In general, the magnetic coupling strengths are stronger for shorter bonds. Ho(2) spins are expected to order at higher temperatures or at least at the same temperature with Ho(1) spins. The low ordering temperature and the reduced magnetic Ho(2) moment value could be the direct result of the geometric magnetic frustration, assuming the $J_{\text{Ho}(2)-\text{Ho}(2)}$ are antiferromagnetic. Considering the small and negative Curie-Weiss temperature,

ferromagnetic ordering of Ho(1) sublattice, and 12 Ho(1)-Ho(1) bonds vs three or four Ho(2)-Ho(2) bonds, $J_{\text{Ho}(2)-\text{Ho}(2)}$ indeed should be antiferromagnetic and three to four times stronger than $J_{\text{Ho}(1)-\text{Ho}(1)}$. The ferromagnetic moment of the Ho(1) spins contribute to the quick rise in the low-field regime of $M(H)$, whereas the nonsaturation in $\text{Ho}_5\text{Co}_6\text{Sn}_{18}$ is due to both the antiferromagnetic $J_{\text{Ho}(2)-\text{Ho}(2)}$ couplings and in-plane magnetic anisotropy. This is in contrast to the spin-ice $\text{Ho}_2\text{Ti}_2\text{O}_7$, characterized by the ferromagnetic coupling and local Ising anisotropy along the $\langle 1\,1\,1 \rangle$ directions, reaches the saturation moment at $H_a \sim 80$ kOe [30].

We observe the QENS signals at $q = 0.52\,\text{Å}^{-1}$ at $T = 5$ K, and they are significantly weaker at $T = 1.6$ K, at which the Ho(2) spins are essentially disordered. Considering the
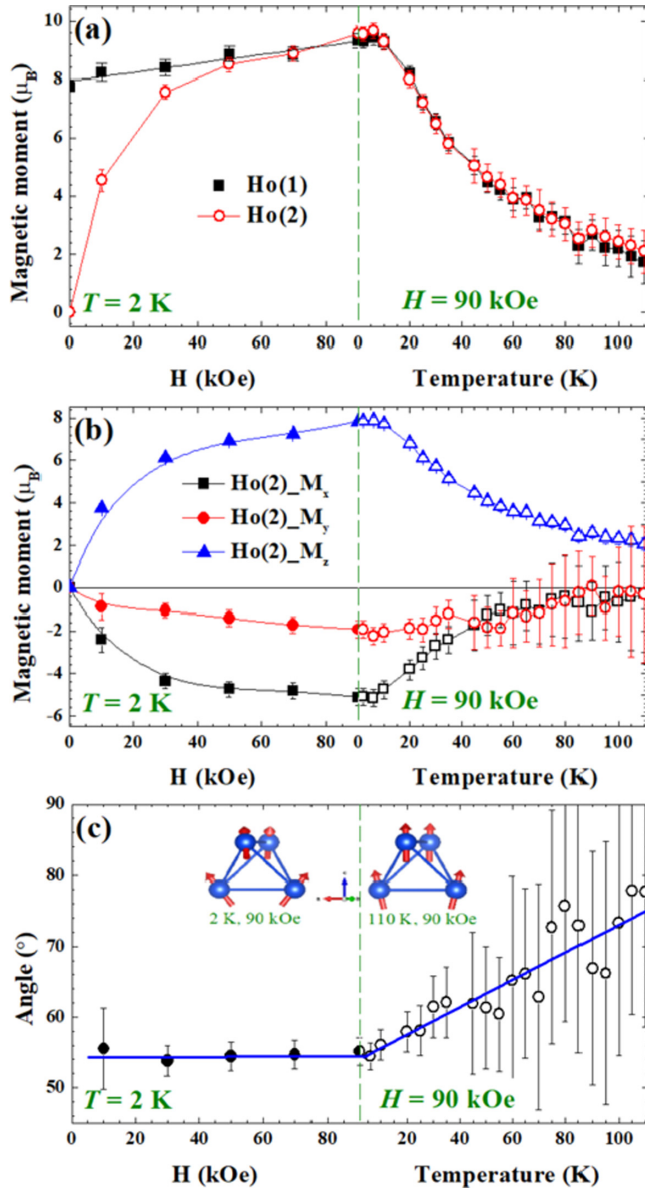
FIG. 9. The refined magnetic moments from the NPD patterns collected under various fields and temperatures. (a) Modulus of the magnetic moments of Ho(1) and Ho(2), (b) the $M_x$, $M_y$, and $M_z$ components of Ho(2), (c) the angle between the Ho(2) and the $a$-$b$ plane.

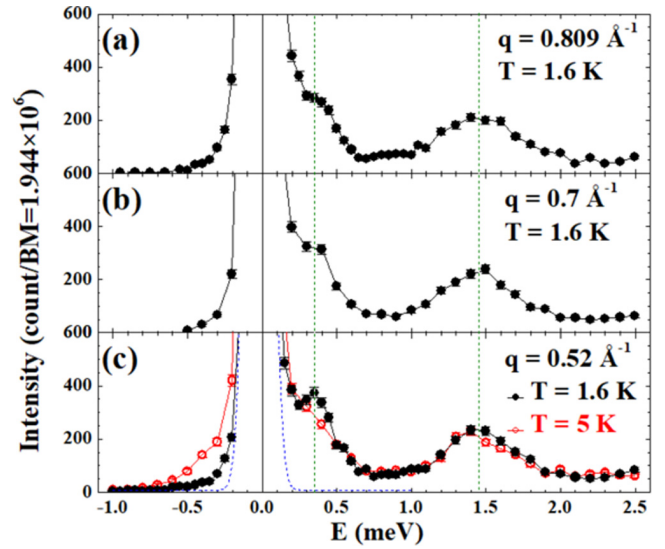spectrum weight of the QENS at 1.6 and 5 K, the major contribution to the QENS should come from the Ho(1) spins.



FIG. 10. Constant-$q$ energy scans measured on a polycrystalline sample at 1.6 K at various q positions. (a) (1 1 2) peak, $q = 0.809\,\text{Å}^{-1}$, (b) $q = 0.7\,\text{Å}^{-1}$, and (c) $q = 0.52\,\text{Å}^{-1}$. CEF excitations from $Ho^{3+}$ are observed at $E = 0.345(4)$ and $1.467(11)$ meV. The scan at $q = 0.52\,\text{Å}^{-1}$, $T = 5\,\text{K}$ shows quasielastic scattering. The dotted line indicates the instrumental resolution of 0.15 meV.

It is reported in some other phase II compounds that the $8b$ rare-earth site could be either deficient or partially replaced by the tin, which makes it more like a disordered fluorite structure [31,32]. We argue that a significant amount of disorder can lead to a dynamic ground state when combined with frustration at low temperatures, which could be the origin of the magnetic QENS.

[1] R. Moessner and A. P. Ramirez, Geometrical frustration, Phys. Today **59**(2), 24 (2006).

[2] J. S. Gardner, M. K. P. Gingras, and J. E. Greedan, Magnetic pyrochlore oxides, Rev. Mod. Phys. **82**, 53 (2010).

[3] M. J. Harris, S. T. Bramwell, D. F. McMorrow, T. Zeiske, and K. W. Godfrey', Geometrical Frustration in the Ferromagnetic Pyrochlore Ho$_2$Ti$_2$O$_7$, Phys. Rev. Lett. **79**, 2554 (1997).

[4] T. Fennell, O. A. Petrenko, B. Fåk, S. T. Bramwell, M. Enjalran, T. Yavors'kii, and M. J. P. Gingras, R. G. Melko, and G. Balakrishnan, Neutron scattering investigation of the spin ice state in Dy$_2$Ti$_2$O$_7$, Phys. Rev. B **70**, 134408 (2004).

[5] S.-W. Han, J. S. Gardner, and C. H. Booth, Structural properties of the geometrically frustrated pyrochlore Tb$_2$Ti$_2$O$_7$, Phys. Rev. B **69**, 024416 (2004).

[6] T. Taniguchi, T. Munenaka, and H. Sato, Spin glass behavior in metallic pyrochlore ruthenate Ca$_2$Ru$_2$O$_7$, J. Phys.: Conf. Ser. **145**, 012017 (2009).

[7] S. T. Bramwell and M. J. P. Gingras, Spin ice state in frustrated magnetic pyrochlore materials, Science **294**, 1495 (2001).

[8] J. P. Remeika, G. P. Espinosa, A. S. Cooper, H. Barz, J. M. Rowell, D. B. McWhan, J. M. Vandenberg, D. E. Moncton, Z. Fisk, L. D. Woolf, H. C. Hamaker, M. B. Maple, G. Shirane, and W. Thomlinson, A new family of ternary intermetallic superconducting/magnetic stannides, Solid State Commun. **34**, 923 (1980).

[9] X.-W. Lei, G.-H. Zhong, C.-L. Hu, and J.-G. Mao, Syntheses and crystal structures of $Y_7Co_6Sn_{23}$ and $RE_5Co_6Sn_{18}$ (RE = Sc, Ho), J. Alloys Compd. **485**, 124 (2009).

[10] M. Feig, L. Akselrud, W. Schnelle, V. Dyadkin, D. Chernyshov, A. Ormeci, P. Simon, A. Leithe-Jasper, and R. Gumeniuk, Crystal structure, chemical bonding, electrical and thermal transport in $Sc_5Rh_6Sn_{18}$, Dalton Trans. **49**, 6832 (2020).

[11] Ed. K. Okudzeto, E. L. Thomas, M. Moldovan, D. P. Young, and J. Y. Chan, Magnetic properties of the single crystal stannides $Ln_7Co_6Sn_{23}$ (Ln = Dy, Ho) and $Ln_5Co_6Sn_{18}$ (Ln = Er, Tm), Physica B (Amsterdam, Neth.) **403**, 1628 (2008).

[12] K. Andres, J. P. Remeika, G. P. Espinosa, and A. S. Cooper, Low-field magnetization studies in the reentrant superconductor $ErRh_{1.1}Sn_{3.6}$, Phys. Rev. B **23**, 1179 (1981).

[13] F. J. Lázaro, A. W. M. van de Pasch, and J. Flokstra, Spin glass behaviour in the rare earth ternary stannide $HoRh_{1.2}Sn_{3.9}$, J. Magn. Magn. Mater. **71**, 10 (1987).

[14] Y. Chen, B. He, J. He, W. He, L. Zeng, and L. Nong, Crystal structure, properties, and diffraction data of a new compound $Dy_5Co_6Sn_{18}$, Powder Diffr. **23**, 26 (2008).

[15] W. J. Zeng, Y. Q. Chen, W. He, and C. Zeng, Advances in Engineering Materials and Applied Mechanics, in *Proceedings of the International Conference on Machinery, Materials Science and Engineering Application (MMSE 2015), Wuhan, China*, edited by G. Zhang, Q. Gao, and Q. Xu (Taylor & Francis Group, London, 2015).

[16] C. N. Kuo, C. W. Tseng, C. M. Wang, C. Y. Wang, Y. R. Chen, L. M. Wang, C. F. Lin, K. K. Wu, Y. K. Kuo, and C. S. Lue, Lattice distortion associated with Fermi-surface reconstruction in $Sr_3Rh_4Sn_{13}$, Phys. Rev. B **91**, 165141 (2015).

[17] M. Avdeev and J. R. Hester, ECHIDNA: A decade of high-resolution neutron powder diffraction at OPAL, J. Appl. Crystallogr. **51**, 1597 (2018).

[18] A. J. Studer, M. E. Hagen, and T. J. Noakes, Wombat: The high-intensity powder diffractometer at the OPAL reactor, Physica B (Amsterdam, Neth.) **385-386**, 1013 (2006).

[19] J. Rodriguez-Carvajal, Recent advances in magnetic structure determination by neutron powder diffraction, Physica B (Amsterdam, Neth.) **192**, 55 (1993).

[20] M. I. Aroyo, J. M. Perez-Mato, D. Orobengoa, E. Tasci, G. de la Flor, and A. Kirov, Crystallography online: Bilbao crystallographic server, Bulg. Chem. Commun. **43**, 183 (2011).

[21] M. I. Aroyo, J. M. Perez-Mato, C. Capillas, E. Kroumova, S. Ivantchev, G. Madariaga, A. Kirov, and H. Wondratschek, Bilbao Crystallographic Server I: Databases and crystallographic computing programs, Z. Kristallogr. **221**, 15 (2006).

[22] M. I. Aroyo, A. Kirov, C. Capillas, J. M. Perez-Mato, and H. Wondratschek, Bilbao Crystallographic Server II: Representations of crystallographic point groups and space groups, Acta Crystallogr. **A62**, 115 (2006).

[23] C.-M. Wu, G. Deng, J. S. Gardner, P. Vorderwisch, W.-H. Li, S. Yano, J.-C. Peng, and E. Imamovicc, SIKA-the multiplexing cold-neutron triple-axis spectrometer at ANSTO, JINST **11**, P10009 (2016).

[24] Y. Shinichiro, G. N. Iles, J.-Ch. Peng, and Ch.-M. Wu, Current status of the taiwanese cold triple axis spectrometers, SIKA, at ANSTO, J. Synch. Investig. **14**, S207 (2020).

[25] C. W. Wang, J. W. Lin, C. S. Lue, H. F. Liu, C. N. Kuo, R. A. Mole, and J. S. Gardner, Magnetic correlations in the intermetallic antiferromagnet $Nd_3Co_4Sn_{13}$, J. Phys.: Condens. Matter **29**, 435801 (2017).

[26] J. G. A. Ramon, C. W. Wang, L. Ishida, P. L. Bernardo, M. M. Leite, F. M. Vichi, J. S. Gardner, and R. S. Freitas, Absence of spin-ice state in the disordered fluorite $Dy_2Zr_2O_7$, Phys. Rev. B **99**, 214442 (2019).

[27] W. S. Corak and C. B. Satterthwaite, Atomic heats of normal and superconducting tin between 1.2 ° and 4.5 °K, Phys. Rev. **102**, 662 (1956).

[28] See Supplemental Material at http://link.aps.org/supplemental/10.1103/PhysRevB.105.104429 for details on the structural refinement, magnetization curves at various temperatures of the polycrystalline sample, and neutron powder diffraction patterns of the sample containing isopropanol ice.

[29] A. P. Ramirez, Strongly geometrically frustrated magnets, Annu. Rev. Mater. Sci. **24**, 453 (1994).

[30] A. L. Cornelius and J. S. Gardner, Short-range magnetic interactions in the spin-ice compound $Ho_2Ti_2O_7$, Phys. Rev. B **64**, 060406(R) (2001).

[31] S. Miyaglia, J. L. Hodeau, F. de Bergevin, and M. Marezio, Structural studies by electron and x-ray diffraction of the disordered phasee II': $(Sn_{1-x}Tb_x)$ $Tb_4Rh_6Sn_{18}$ and $(Sn_{1-x}Dy_x)$ $Dy_4Os_6Sn_{18}$, Acta Crystallogr. **B43**, 76 (1987).

[32] B. Ya. Kotur and R. Černy, Disordered microtwinned $(Sc_{1-x})Sc_4Co_6Sn_{18}(x = 0.14)$, Croat. Chem. Acta **72**, 2 (1999).